Electronic Supplementary Material (ESI) for Soft Matter.
This journal is © The Royal Society of Chemistry 2020

Supplementary Information:
Tuning the Selective Permeability of Polydisperse Polymer Networks

Won Kyu Kim,[1,*] Richard Chudoba,[2,3] Sebastian Milster,[2,4]
Rafael Roa,[5] Matej Kanduč,[6] and Joachim Dzubiella[2,4,7,†]

[1]Korea Institute for Advanced Study, Seoul 02455, Republic of Korea
[2]Research Group for Simulations of Energy Materials,
Helmholtz-Zentrum Berlin für Materialien und Energie, D-14109 Berlin, Germany
[3]Division of Theoretical Chemistry, Department of Chemistry,
Lund University, P.O. Box 124, SE-22100 Lund, Sweden
[4]Applied Theoretical Physics-Computational Physics, Physikalisches Institut,
Albert-Ludwigs-Universität Freiburg, D-79104 Freiburg, Germany
[5]Departamento de Física Aplicada I, Facultad de Ciencias, Universidad de Málaga, E-29071 Málaga, Spain
[6]Jožef Stefan Institute, SI-1000 Ljubljana, Slovenia
[7]Cluster of Excellence livMatS @ FIT - Freiburg Center for Interactive Materials and Bioinspired Technologies,
Albert-Ludwigs-Universität Freiburg, D-79110 Freiburg, Germany

I. COMPUTER SIMULATIONS AND SUPPORTING RESULTS

A. Mean concentration profiles of networks and penetrants

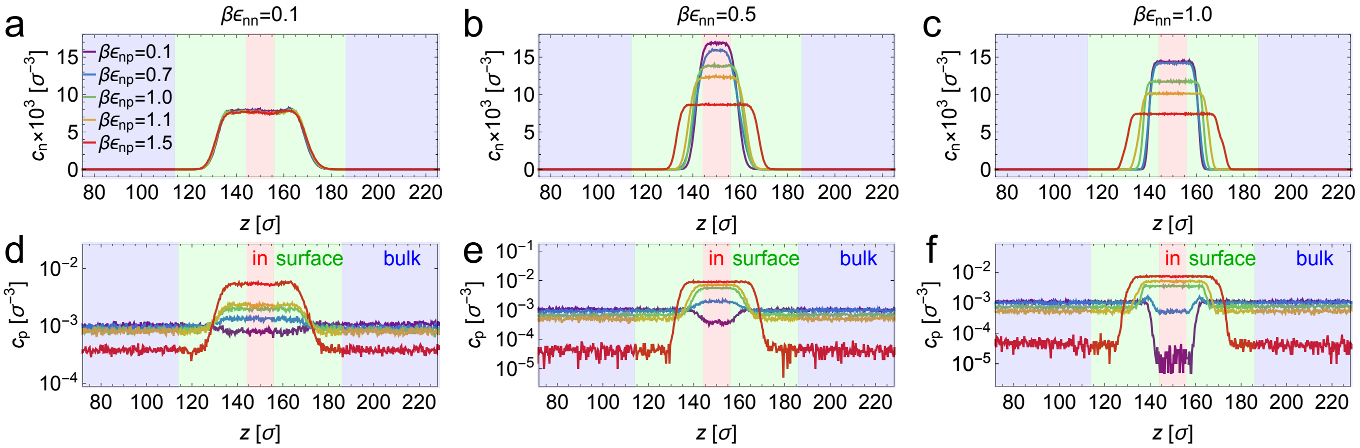

FIG. S1. Upper panels: network monomer concentration $c_\mathrm{n}(z)$ in a good ((a) $\beta\epsilon_\mathrm{nn} = 0.1$), intermediate ((c) $\beta\epsilon_\mathrm{nn} = 0.5$), and poor solvent ((c) $\beta\epsilon_\mathrm{nn} = 1.0$) with different network–penetrant interactions $\beta\epsilon_\mathrm{np}$. Lower panels: penetrant concentration $c_\mathrm{p}(z)$ in (d) the good, (e) intermediate, and (f) poor solvent with different network–penetrant interactions $\beta\epsilon_\mathrm{np}$. Three regions (in, surface, and bulk) are depicted in each plot by different colors, where we sampled the partitioning in the region "in".

We show in Fig. S1 the mean concentration profiles of the polymer network monomers and the penetrants in the longitudinal direction z. The upper panels depict the network monomer concentrations $c_\mathrm{n}(z)$ in corresponding good ($\beta\epsilon_\mathrm{nn} = 0.1$), intermediate ($\beta\epsilon_\mathrm{nn} = 0.5$), and poor solvent ($\beta\epsilon_\mathrm{nn} = 1.0$) regimes, for different network–penetrant attractions $\beta\epsilon_\mathrm{np}$. The lower panels depict the penetrant concentrations $c_\mathrm{p}(z)$ in a similar manner. We show three regions (in, surface, and bulk) by different colors in each plot, where we sampled the partitioning in the region "in". After examining the overall plateau of the concentration profiles, we decided that the "in" region can be defined by the longitudinal distance of around $10\ \sigma = 4$ nm, centered at the center-of-mass position of the membrane monomers. The "surface" regions are determined by the longitudinal distance of $25\sigma = 10$ nm, next to the "in" region.

---

[*] wonkyukim@kias.re.kr
[†] joachim.dzubiella@physik.uni-freiburg.de

B. Cross-linker radial distribution functions

We show in Fig. S2 the two-dimensional radial distribution function $g_{\text{xlink}}^{\text{2D}}(r)$ between cross-linkers (xlink) in the network for different values of ϕ_{n} and ϵ_{np}. The pair correlation functions were computed by averaging within thin membrane slabs (of thickness 1σ) in the x and y directions, and finally averaged over all slabs. The number of the membrane slabs ranges from 18 to 38, depending on the whole membrane width (see Fig. S1).

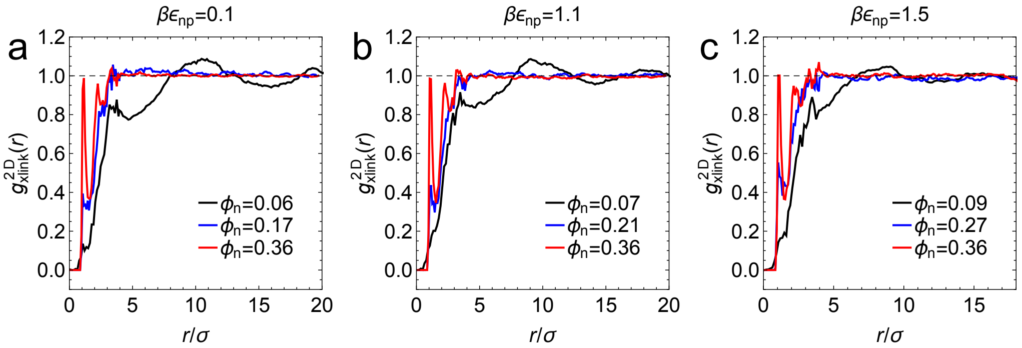

FIG. S2. Two-dimensional radial distribution functions $g_{\text{xlink}}(r)$ between the cross-linkers for different values of ϕ_{n} and ϵ_{np}.

C. Virial coefficients for partitioning

In Table S1 we show the virial coefficients B_2^{np} and B_3^{nnp} obtained from fitting the partitioning $\mathcal{K}(\phi_{\text{n}})$ in Fig. 3a in the main text by the virial expression eqn (2) in the main text.

We show in Table S1 the fitted second virial coefficients B_2^{np} in comparison with B_2^{LJ} for the LJ interaction:

$$B_2^{\text{LJ}}(\epsilon_{\text{np}}) = \int_0^\infty \mathrm{d}r 2\pi r^2 [1 - \exp(-\beta U_{\text{LJ}}^{\text{np}}(r, \epsilon_{\text{np}}))], \tag{S1}$$

where we use the length parameter $\sigma_{\text{nn}} = \sigma_{\text{np}} = \sigma$.

In a similar manner we show the fitted third virial coefficients B_3^{np} in comparison with B_3^{LJ} for the one-component LJ interaction:

$$B_3^{\text{LJ}}(\epsilon) = -\frac{1}{3} \int_{\mathcal{V}} \int_{\mathcal{V}} \mathrm{d}^3\mathbf{r}_{12} \mathrm{d}^3\mathbf{r}_{13} [1 - \exp(-\beta U_{\text{LJ}}(r_{12}, \epsilon))][1 - \exp(-\beta U_{\text{LJ}}(r_{13}, \epsilon))][1 - \exp(-\beta U_{\text{LJ}}(r_{23}, \epsilon))], \tag{S2}$$

where $\mathcal{V}$ is the total volume.

D. Partitioning and mean penetrant number inside the network for large attractions

In Figs. S3a and b, the partitioning $\log_{10} \mathcal{K}$ is shown vs. ϵ_{nn} and ϕ_{n} for various interaction strengths, ranging from low $\epsilon_{\text{np}} = 0.1\ k_{\text{B}}T$ to high $\epsilon_{\text{np}} = 2\ k_{\text{B}}T$. For large network–penetrant attraction and dense packing, simulation

TABLE S1. Virial coefficients B_2^{np} and B_3^{nnp} in eqn (2) obtained as fitting parameters in Fig. 3a are shown for different values of ϵ_{np}. The exact values of B_2^{LJ} and B_3^{LJ} for LJ potential are shown for comparison.

$\beta\epsilon_{\text{np}}$	0.1	0.7	1.0	1.1	1.2	1.5
B_2^{np}/σ^3	0.63 ± 0.08	-2.25 ± 0.17	-4.82 ± 0.19	-5.61 ± 0.16	-6.52 ± 0.21	-9.26 ± 0.34
B_2^{LJ}/σ^3	0.97	-2.77	-5.32	-6.27	-7.29	-10.75
$B_3^{\text{nnp}}/\sigma^6$	3.85 ± 0.35	4.74 ± 0.44	6.85 ± 0.45	7.46 ± 0.38	8.31 ± 0.48	10.41 ± 0.74
B_3^{LJ}/σ^6	1.25	2.46	1.89	0.55	-1.92	-22.07

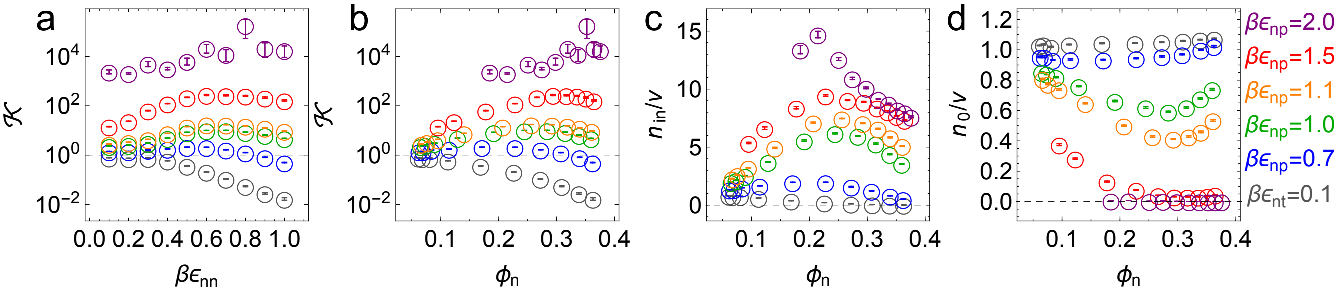

FIG. S3. Partitioning $\log_{10}\mathcal{K}$ as a function of (a) $\epsilon_{\rm nn}$ and (b) $\phi_{\rm n}$, up to a high attraction of $\epsilon_{\rm np} = 2\ k_{\rm B}T$. (c) Mean penetrant number $n_{\rm in}$ per unit volume inside the network as a function of the polymer volume fraction $\phi_{\rm n}$. (d) Mean penetrant number n_0 per unit volume outside the network, as a function of the polymer volume fraction $\phi_{\rm n}$.

results become noisy. This is due to strong confinement effects, which result in nonequilibrium metastable states. In Fig. S3c we show the mean penetrant number $n_{\rm in}$ per unit volume $v \equiv V(\epsilon_{\rm nn}, \epsilon_{\rm np})/1000$ inside the network, which is also maximized with respect to $\phi_{\rm n}$. The mean penetrant number n_0 per v outside the network, on the other hand, shown in Fig. S3d, is minimized with respect to $\phi_{\rm n}$.

E. Lateral length of simulation box L_x and L_y in equilibrium

In Table S2, we show values of the lateral length of the simulation box L_x $(=L_y)$ for several chosen interaction parameters $\epsilon_{\rm nn}$ and $\epsilon_{\rm np}$. We computed L_x from the production run data, and the presented values are the mean as well as the standard deviation in the parentheses.

TABLE S2. Lateral length of the simulation box $L_x(= L_y)$ in units of σ for different interaction parameters $\epsilon_{\rm nn}$ and $\epsilon_{\rm np}$. The presented values are mean with standard deviation in the parentheses, which are computed from the production run data.

$\beta\epsilon_{\rm nn}$ $\beta\epsilon_{\rm np}$	0.1	0.5	1.0
0.1	52.18(0.06)	41.98(0.10)	27.08(0.17)
1.1	49.32(0.09)	33.49(0.24)	23.21(0.28)
1.5	41.40(0.19)	25.45(0.19)	19.96(0.14)

F. Calculations of diffusivity inside the network

To calculate the penetrant diffusivity in the membrane, $D_{\rm in}$, we generated 20 simulation set ups with 3D periodic boundary conditions of the polydisperse tetra-functional networks including the penetrants for each parameter set of $\epsilon_{\rm nn}$ and $\epsilon_{\rm np}$, as shown in Fig. S4. To determine the cubic box size and the number of the penetrants in the cell, we used the equilibrium values of the penetrant density and the polymer density obtained from the main simulation data from the anisotropic setups. We carried out the simulations typically for 10^4 time steps. We computed the mean-squared-displacement (MSD) of the penetrants in the networks, averaged over time and particles, [1] as shown in Fig. S5 (upper panels), within the dimensionless simulation time range from $t = 100$ to $t = 1000$ to obtain diffusivity via $\mathrm{MSD} = 6D_{\rm in}t$, ensuring the normal diffusion, [1] which fulfills $\alpha = \frac{\mathrm{d}\ln \mathrm{MSD}}{\mathrm{d}\ln t} = 1$ in Fig. S5 (lower panels).

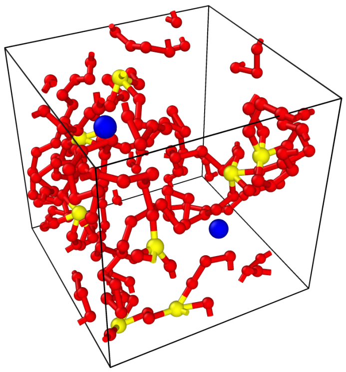

FIG. S4. Simulation snapshot of the polydisperse tetra-functional network with penetrants (blue) used to calculate the penetrant diffusivity $D_{\rm in}$.

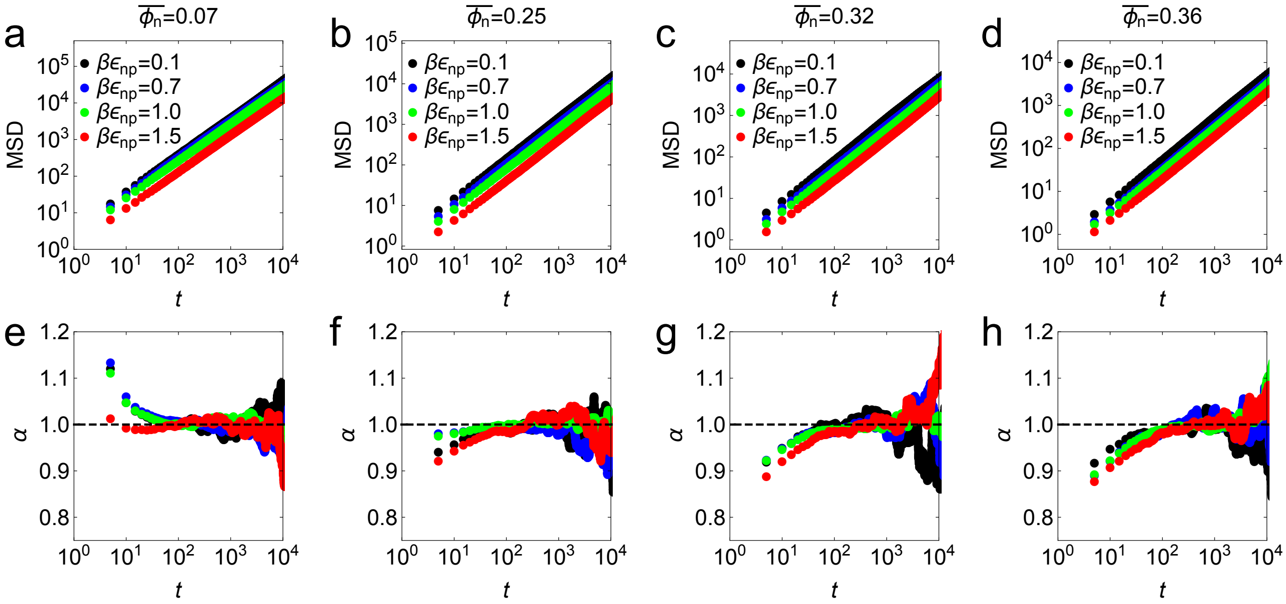

FIG. S5. Upper panels: Mean-squared-displacement (MSD(t)) of the penetrants in the networks. Lower panels: α is the local slope of the MSD, defined as the numerical derivative $\mathrm{d}\ln\mathrm{MSD}/\mathrm{d}\ln t$.

G. Membrane isotropy in the central region

There occur finite size effects on the network conformation, particularly involved with attractive penetrants, which eventually causes the global anisotropy of the network. The desired network region suitable for sampling the diffusivity $D_{\rm in}$ is the central region, where the network concentration profile reaches a plateau in the z direction, corresponding to the "in" region shown in Fig. S1.

To check the anisotropy of the "in" region, we calculated the shape descriptor κ^2 for three different quantities. In general, there are three representative limiting cases of the order parameter κ^2; 3D isotropic ($\kappa^2 = 0$), anisotropic on a plane ($\kappa^2 = 0.25$), and anisotropic on a line ($\kappa^2 = 1$), as depicted by the dashed lines in Fig. S6a.

We first calculated the relative shape anisotropy $\kappa^2_{\rm shape}$ of the network monomer and cross-linker positions in the central "in" region, for several chosen parameters. The relative shape anisotropy $\kappa^2_{\rm shape}$ is defined as [2]

$$\kappa^2_{\rm shape} = \frac{3}{2}\frac{\lambda_x^4+\lambda_y^4+\lambda_z^4}{(\lambda_x^2+\lambda_y^2+\lambda_z^2)^2} - \frac{1}{2}, \tag{S3}$$

where λ_x, λ_y, and λ_z are the principal moments of the gyration tensor of positions of $N_{\rm n}$ network particles, defined

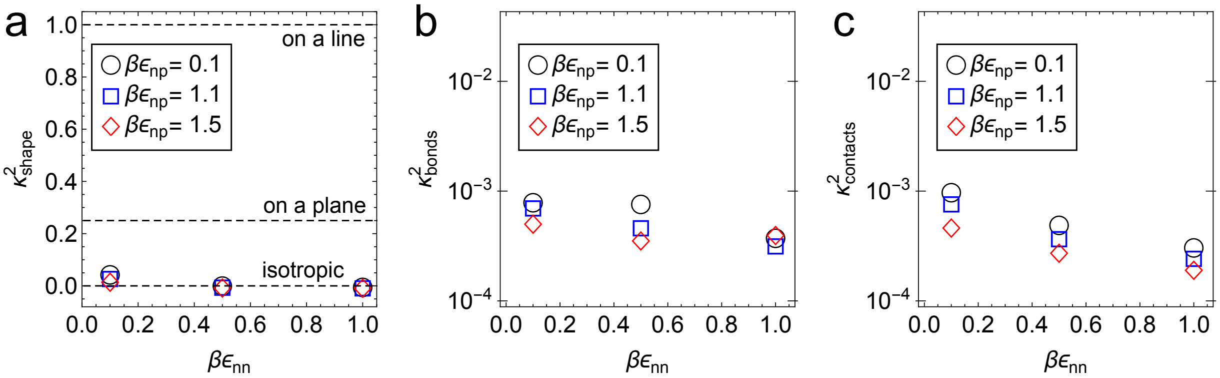

FIG. S6. (a) The relative shape anisotropy of the network $\kappa^2_{\rm shape}$ as a function of the interaction parameters $\epsilon_{\rm nn}$ for different $\epsilon_{\rm np}$. The dashed lines depict three representative limiting cases; 3D isotropic ($\kappa^2 = 0$), on a plane ($\kappa^2 = 0.25$), and on a line ($\kappa^2 = 1$). (b) The bond orientation anisotropy of the network $\kappa^2_{\rm bonds}$ as a function of the interaction parameters $\epsilon_{\rm nn}$ for different $\epsilon_{\rm np}$. (c) The local orientation anisotropy of the network $\kappa^2_{\rm contacts}$ as a function of the interaction parameters $\epsilon_{\rm nn}$ for different $\epsilon_{\rm np}$. All results are averaged over independent simulation runs with the error bars smaller than the symbol size.

as

$$S_{ij} = \frac{1}{2N_{\rm n}^2}\sum_{k=1}^{N_{\rm n}}\sum_{l=1}^{N_{\rm n}}\left({r_i}^{(k)} - {r_i}^{(l)}\right)\left({r_j}^{(k)} - {r_j}^{(l)}\right), \tag{S4}$$

where $i, j \in \{x, y, z\}$, $\vec{r}^{(k)}$ and $\vec{r}^{(l)}$ are the particle positions. We sampled $\kappa^2_{\rm shape}$ of the network monomer and the cross-liker positions in a cubic box of the volume $= 10^3\ \sigma^3$ centered at each "in" region, and averaged over time in equilibrium. Figure S6a shows that the relative shape of the network in the central region is very isotropic over all chosen nine representative parameter values.

In addition, we employed two more methods to confirm the local isotropy in the entire "in" region of the simulated polymer membranes. The second method is based on the same calculation given in eqn (S3), but evaluates the bond anisotropy $\kappa^2_{\rm bonds}$ using the gyration tensor of bond orientations, defined as

$$S_{ij} = \frac{1}{N_{\rm bonds}}\sum_{k=1}^{N_{\rm bonds}}\frac{b_i^{(k)} b_j^{(k)}}{|\vec{b}^{(k)}|^2}. \tag{S5}$$

We sampled the bond vectors $\vec{b}$ of all network bonds $N_{\rm bonds}$ in the entire "in" region and averaged over time.

The third method defines the local orientation anisotropy $\kappa^2_{\rm contacts}$. It is based on the same calculation given in eqn (S3) and eqn (S4), but the relative positions $\vec{r}^{(k)} - \vec{r}^{(l)}$ were normalized to obtain the relative orientations. The relative orientation of two polymer beads k and l was sampled for all possible combinations (bonded and non-bonded) within a cut-off of 2.5 σ and only in the entire "in" region. Note that this approach is similar to the evaluation of the fabric tensor in granular materials science, [3] where normalized contact vectors are computed. We have checked that the change of the cut-off distance did not significantly change the result.

The results for the representative parameters are shown in Figs. S6b and S6c. All different methods we applied signify the local isotropy in the central network region, *i.e.*, $\kappa^2 \approx 0$ despite the apparent global deformation of the network membrane. Therefore, the above analysis justifies the use of isotropic networks in the auxiliary simulations for the calculation of the diffusion coefficients.

H. Effects of different penetrant bulk concentrations

In Fig. S7 we show the effect of penetrant concentration on the partitioning. Upon increasing the penetrant number $N_{\rm p}$ by two times, the partitioning with the low attraction $\beta\epsilon_{\rm np} = 0.1$ becomes larger as the network volume fraction $\phi_{\rm n}$ increases, while it becomes smaller with the large attraction $\beta\epsilon_{\rm np} = 1.5$. However, an overall characteristic behavior of the partitioning is qualitatively similar.

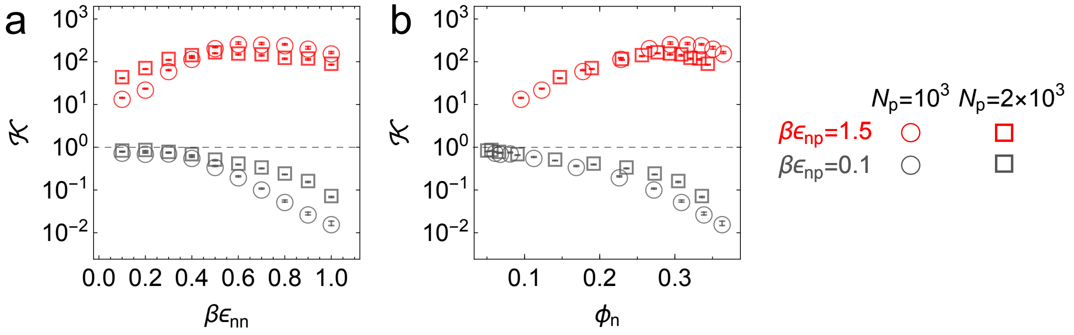

FIG. S7. Effects of different penetrant concentrations on the partitioning $\log_{10}\mathcal{K}$ vs. (a) $\epsilon_{\rm nn}$ and (b) $\phi_{\rm n}$ for the different total number of penetrants, $N_{\rm p} = 10^3$ (circles) and $N_{\rm p} = 2\times10^3$ (rectangles), and for the network–penetrant interaction values of $\beta\epsilon_{\rm np} = 0.1$ (gray) and $\beta\epsilon_{\rm np} = 1.5$ (red).

I. Network (slab membrane) volume

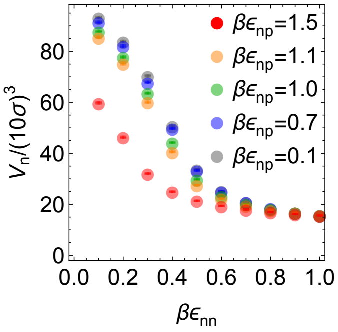

FIG. S8. Total network (slab) volume $V_{\rm n}$ as a function of the solvent quality $\epsilon_{\rm nn}$ for different values of the network–penetrant interaction $\epsilon_{\rm np}$.

In Fig. S8 we show the network slab volume $V_{\rm n}$ as a function of the solvent quality $\epsilon_{\rm nn}$. As $\epsilon_{\rm nn}$ increases the volume decays rapidly until around $\epsilon_{\rm nn} = 0.5\ k_{\rm B}T$. As the network–penetrant interaction energy $\epsilon_{\rm np}$ increases up to $\epsilon_{\rm np} = 1.5\ k_{\rm B}T$, the volume considerably decreases, indicating the onset of the penetrant-induced collapse. [4] We calculate the polymer volume fraction using $\phi_{\rm n} = (N_{\rm m} + N_{\rm xlink})v_0/V_{\rm n}$, where $v_0 = \pi\sigma^3/6$ is the monomer volume with the diameter $\sigma = \sigma_{\rm nn} = \sigma_{\rm np}$.

J. Scaling theories for the penetrant diffusivity

In Fig. S9 we compare the simulation results (symbols) with various scaling theories (solid curves) for the penetrant diffusivity in the polymer networks. In Fig. S9a we show the free-volume theory [5–11]

$$D_{\rm in}/D_0 = b{\rm e}^{-c\left(\frac{\phi_{\rm n}}{1-\phi_{\rm n}}\right)}. \tag{S6}$$

In Fig. S9b we show the hydrodynamic/obstruction theory [11, 12]

$$D_{\rm in}/D_0 = {\rm e}^{-a(\phi_{\rm n})^{\nu}}. \tag{S7}$$

In Fig. S9c we show the extended barrier-crossing theory [13, 14]

$$D_{\rm in}/D_0 = \frac{1}{1+\alpha{\rm e}^{\beta\epsilon_{\rm np}}\left(\phi_{\rm n}\right)^{\zeta}}. \tag{S8}$$

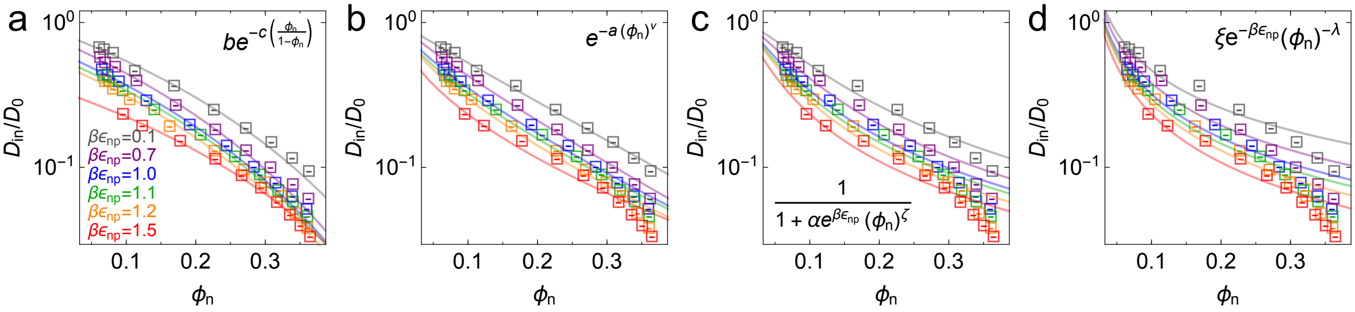

FIG. S9. Penetrant diffusivity in polymer networks compared with various scaling theories. (a) Free-volume theory (as shown in the main text), (b) hydrodynamic/obstruction theory, (c) extended barrier-crossing theory, (d) barrier-crossing theory. See Table S3 for the fitting parameters.

In Fig. S9d we show the barrier-crossing theory [14, 15]

$$D_{\mathrm{in}}/D_0 = \xi \mathrm{e}^{-\beta\epsilon_{\mathrm{np}}} \left(\phi_{\mathrm{n}}\right)^{-\lambda} . \tag{S9}$$

TABLE S3. Parameters in the scaling theories shown in Fig. S9, fitted from the simulation data.

$\beta\epsilon_{\mathrm{np}}$	0.1	0.7	1.0	1.1	1.2	1.5
b	0.86 ± 0.02	0.76 ± 0.02	0.63 ± 0.02	0.57 ± 0.01	0.53 ± 0.02	0.34 ± 0.01
c	4.17 ± 0.19	4.81 ± 0.16	4.77 ± 0.19	4.69 ± 0.18	4.79 ± 0.20	3.87 ± 0.09
a	6.10 ± 0.30	6.43 ± 0.23	5.98 ± 0.22	5.83 ± 0.23	5.96 ± 0.22	5.35 ± 0.35
ν	0.98 ± 0.03	0.88 ± 0.02	0.76 ± 0.02	0.71 ± 0.02	0.69 ± 0.02	0.56 ± 0.04
α	29.71 ± 4.51	22.55 ± 4.07	18.21 ± 3.13	17.35 ± 3.06	18.42 ± 3.15	14.61 ± 3.21
ζ	1.54 ± 0.07	1.50 ± 0.08	1.40 ± 0.07	1.37 ± 0.08	1.39 ± 0.07	1.30 ± 0.11
ξ	0.07 ± 0.01	0.08 ± 0.02	0.09 ± 0.02	0.08 ± 0.02	0.08 ± 0.01	0.08 ± 0.02
λ	0.87 ± 0.08	0.97 ± 0.09	1.01 ± 0.08	1.02 ± 0.08	1.08 ± 0.08	1.11 ± 0.11

All the fitting parameters are shown in Table S3, and in Fig. 4 in the main text we show the parameters b and c for the free-volume theory, $D_{\mathrm{in}}/D_0 = b\mathrm{e}^{-c\left(\frac{\phi_{\mathrm{n}}}{1-\phi_{\mathrm{n}}}\right)}$ from eqn S6. We note that b is an exponentially decreasing function of ϵ_{np}, while c is rather independent of ϵ_{np}, which leads to our scaling expression for the penetrant diffusivity,

$$D_{\mathrm{in}}/D_0 \sim \mathrm{e}^{-\beta\epsilon_{\mathrm{np}} - c\left(\frac{\phi_{\mathrm{n}}}{1-\phi_{\mathrm{n}}}\right)} . \tag{S10}$$

II. COARSE-GRAINING OF POLYMER BONDED PARAMETERS FROM ALL-ATOM SIMULATIONS

To obtain the parameters for the bonded potentials in our computer simulations, we used all-atom simulation setups of poly(N-isopropylacrylamide) (PNIPAM) chains crosslinked by N,N'-methylenebisacrylamide (BIS), embedded in water at 290 K, from previous work [16] and as shown in Fig. S10. In particular, we set up two different systems. The first one comprises a BIS cross-linker with four PNIPAM monomers, *i.e.*, each BIS' backbone binding site is terminated by one monomer. This system enables the study of the conformations of PNIPAM chains attached to the cross-linker. The second system consist of a single PNIPAM trimer in water and is used to retrieve the bonding and bending information of the polymer chains only.

A. All-atom simulation details

We employed explicit-water, all-atom molecular dynamics simulations with the OPLS-based force-field developed in Refs [16] and [17]. for the aforementioned systems. Twelve different initial configurations of the BIS-PNIPAM molecule were placed in individual cubic boxes (box length ≈ 4 nm) with approximately 6500 water molecules. For

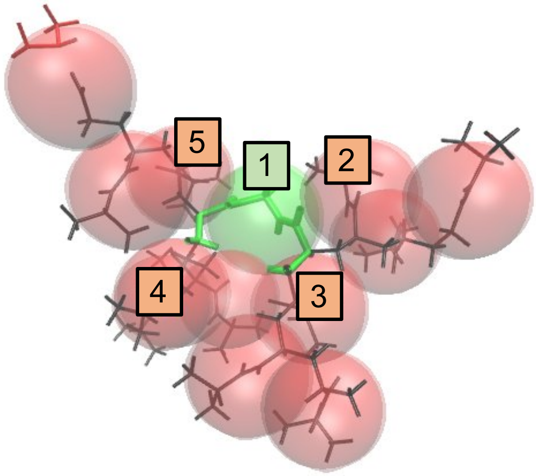

FIG. S10. Illustration of an all-atom and its corresponding coarse-grained (CG) representation of PNIPAM–BIS (poly(N-isopropylacrylamide)–N,N'-methylenebisacrylamide), *i.e.*, one cross-linker and four attached chains with three monomers each. The spheres represent the coarse-grained beads located at the (all-atom) monomers' centers of masses for one cross-linker (green) and the chain (red). In order to obtain the bonded potential parameters used in the main work, two minimal systems were simulated on the all-atom level with explicit water (not shown) at 290 K. The first one consists of one cross-linker (labeled 1) with four PNIPAM monomers (labeled 2, 3, 4, 5), the other one investigates a single PNIPAM trimer.

the PNIPAM trimer we created 17 replicas, each solvated in a box (box length ≈ 2.5 nm) of around 1500 water molecules.

After the initial energy minimization (steepest descent), the system was equilibrated in the NVT ensemble for 2 ns and in the NpT ensemble for an additional 2 ns. The integration step of the leap-frog integrator was set to 2 fs and data were collected every 1 ps during a production simulation time of 100 ns.

The linear constraint solver algorithm [18] was used for all hydrogen bonds, and the SPC/E force-field was used for water molecules. [19] We considered cut-off lengths for LJ and short-range electrostatic interactions as 1 nm. The particle mesh Ewald method with cubic interpolation with a grid spacing of 0.12 nm was used for long-range electrostatics. [20] We used periodic boundary conditions in all three Cartesian directions. The temperature and the pressure in the simulations were controlled by the velocity-rescale thermostat (at temperature $T = 290$ K and the relaxation time constant $\tau_T = 0.1$ ps) and the Berendsen barostat (at pressure $p = 1$ bar and the relaxation time constant $\tau_p = 1$ ps), respectively. [21, 22]

TABLE S4. Bonded parameters in eqns S11 and S12, determined by fitting to all-atom simulation data shown in Fig. S11.

complementary pair	2-1-3 4-1-5	2-1-5 3-1-4	2-1-4 3-1-5
$K_\theta^{\text{m-xlink-m}}/k_\text{B}T$	8.5×10^{-4}	7.2×10^{-4}	2.8×10^{-3}
$\theta_0^{\text{m-xlink-m}}/\text{deg}$	113.4	114.4	80.1
$K_r^{\text{m-xlink}}/(k_\text{B}T/\sigma^2)$	16.4		
$r_0^{\text{m-xlink}}/\sigma$	1.4		
$K_\theta^{\text{m-m-m}}/k_\text{B}T$	1.9×10^{-3}		
$\theta_0^{\text{m-m-m}}/\text{deg}$	98.2		
$K_r^{\text{m-m}}/(k_\text{B}T/\sigma^2)$	34.4		
$r_0^{\text{m-m}}/\sigma$	1.3		

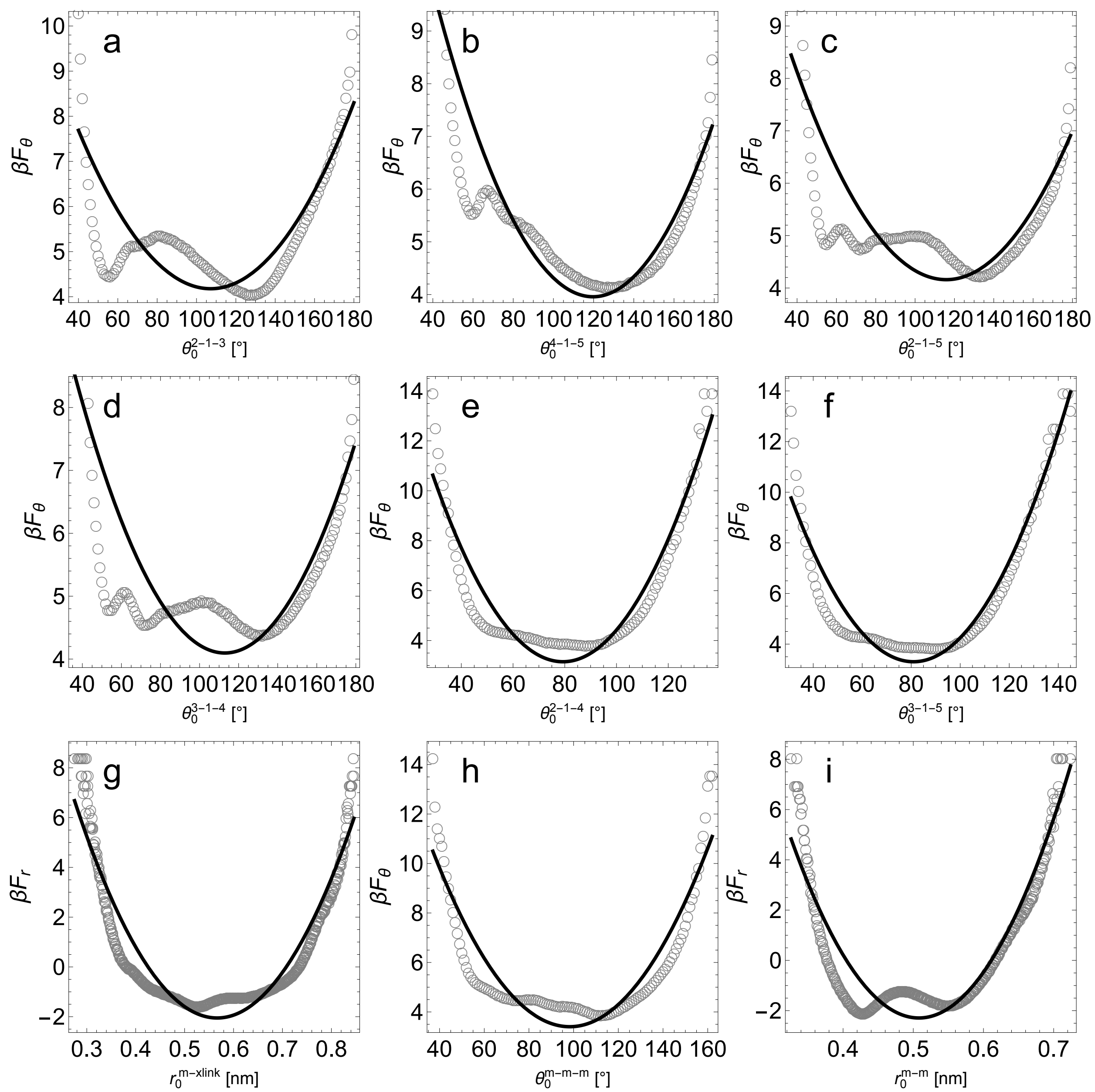

FIG. S11. Free energies (symbols) obtained from the all-atom simulations and fitted harmonic potentials (solid curves) given by eqns S11 and S12. See text for details.

B. Bonded parameters for the polymer networks

In our simulations of the polymer network we considered two-body (stretching) and three-body (bending) bonded potentials, which are approximated as harmonic interactions,

$$F_r^{ij}(r^{ij}) = K_r^{ij}(r^{ij} - r_0^{ij})^2, \tag{S11}$$

$$F_\theta^{ijk}(\theta^{ijk}) = K_\theta^{ijk}(\theta^{ijk} - \theta_0^{ijk})^2, \tag{S12}$$

where $i, j, k = \mathrm{m}$ or xlink is the particle index with m for the PNIPAM monomer and xlink for the BIS cross-linker. There are two stretching potentials $F_r^{\text{m-m}}$ and $F_r^{\text{m-xlink}}$, and since the BIS connects four PNIPAM chains (*i.e.*, tetra-functional) there are six bending potentials in $F_\theta^{\text{m-xlink-m}}$ and one bending potential in $F_\theta^{\text{m-m-m}}$. Therefore, we have nine different bonded potentials in total and we determine eighteen bonded parameters K_r^{ij}, r_0^{ij}, K_θ^{ijk}, and θ_0^{ijk} by fitting to the free energies obtained from the all-atom simulations.

In Fig. S11 the symbols show the free energies F_r and F_θ evaluated from the all-atom simulations, and the solid curves depict the harmonic potentials shown in eqns S11 and S12 with fitted parameters (see Table S4). For analyses we used 12 production trajectories of the PNIPAM–BIS simulations, and 17 production trajectories of the PNIPAM simulations, respectively. The six different bending free energies $F_\theta^{\text{m-xlink-m}}$ at the BIS cross-linker are shown from Figs. S11a to f. These $F_\theta^{\text{m-xlink-m}}$ have three complementary pairs due to the tetra-functional geometry as shown in Fig. S10. We show these three pairs of the bending free energy in Figs. S11a and b for 2-1-3 and 4-1-5 CG monomers, Figs. S11c and d for 2-1-5 and 3-1-4 CG monomers, Figs. S11e and f for 2-1-4 and 3-1-5 CG monomers, respectively. The stretching free energy $F_r^{\text{m-xlink}}$ between CG PNIPAM–BIS monomers is shown in Fig. S11g. The bending $F_\theta^{\text{m-m-m}}$ and the stretching $F_r^{\text{m-m}}$ free energies in CG PNIPAM monomers are shown in Figs. S11h and i, respectively. We compared all the simulation data with the harmonic potentials in eqns S11 and S12, and determined the bonded parameters as shown in Table S4. The thermal energy $k_{\text{B}}T$ and the LJ length $\sigma = 0.4$ nm were used as respective units.

---

[1] J. Shin, A. G. Cherstvy, W. K. Kim, and V. Zaburdaev, Phys. Chem. Chem. Phys. **19**, 18338 (2017).
[2] D. N. Theodorou and U. W. Suter, Macromolecules **18**, 1206 (1985).
[3] P. Fu and Y. F. Dafalias, Int. J. Solids. Struct. **63**, 68 (2015).
[4] W. K. Kim, A. Moncho-Jordá, R. Roa, M. Kanduč, and J. Dzubiella, Macromolecules **50**, 6227 (2017).
[5] H. Yasuda, C. Lamaze, and L. D. Ikenberry, Die Makromol. Chemie **118**, 19 (1968).
[6] H. Yasuda, L. Ikenberry, and C. Lamaze, Die Makromol. Chemie **125**, 108 (1969).
[7] H. Yasuda, A. Peterlin, C. Colton, K. Smith, and E. Merrill, Die Makromol. Chemie **126**, 177 (1969).
[8] N. A. Peppas and C. T. Reinhart, J. Memb. Sci. **15**, 275 (1983).
[9] C. T. Reinhart and N. A. Peppas, J. Memb. Sci. **18**, 227 (1984).
[10] S. R. Lustig and N. A. Peppas, J. Appl. Polym. Sci. **36**, 735 (1988).
[11] B. Amsden, Macromolecules **31**, 8382 (1998).
[12] D. S. Clague and R. J. Phillips, Phys. Fluids **8**, 1720 (1996).
[13] J.-M. Petit, B. Roux, X. Zhu, and P. Macdonald, Macromolecules **29**, 6031 (1996).
[14] L. Masaro and X. Zhu, Prog. Polym. Sci. **24**, 731 (1999).
[15] T. E. Andreoli and J. A. Schafer, *Principles of water and nonelectrolyte transport across membranes* (Springer, 1980).
[16] S. Milster, R. Chudoba, M. Kanduč, and J. Dzubiella, Phys. Chem. Chem. Phys. **21**, 6588 (2019).
[17] V. Palivec, D. Zadrazil, and J. Heyda, arXiv e-prints arXiv:1806.05592 (2018), 1806.05592.
[18] B. Hess, H. Bekker, H. J. C. Berendsen, and J. G. E. M. Fraaije, Journal of Computational Chemistry **18**, 1463 (1997).
[19] H. Berendsen, J. Grigera, and T. Straatsma, Journal of Physical Chemistry **91**, 6269 (1987).
[20] U. Essmann, L. Perera, M. L. Berkowitz, T. Darden, H. Lee, and L. G. Pedersen, J. Chem. Phys. **103**, 8577 (1995).
[21] G. Bussi, D. Donadio, and M. Parrinello, J. Chem. Phys. **126**, 14101 (2007).
[22] H. J. C. Berendsen, J. P. M. Postma, W. F. van Gunsteren, A. DiNola, and J. R. Haak, J. Chem. Phys. **81**, 3684 (1984).